

# PCCP

Accepted Manuscript



This is an *Accepted Manuscript*, which has been through the Royal Society of Chemistry peer review process and has been accepted for publication.

*Accepted Manuscripts* are published online shortly after acceptance, before technical editing, formatting and proof reading. Using this free service, authors can make their results available to the community, in citable form, before we publish the edited article. We will replace this *Accepted Manuscript* with the edited and formatted *Advance Article* as soon as it is available.

You can find more information about *Accepted Manuscripts* in the [Information for Authors](#).

Please note that technical editing may introduce minor changes to the text and/or graphics, which may alter content. The journal's standard [Terms & Conditions](#) and the [Ethical guidelines](#) still apply. In no event shall the Royal Society of Chemistry be held responsible for any errors or omissions in this *Accepted Manuscript* or any consequences arising from the use of any information it contains.

# Flue gas CO<sub>2</sub> mineralization using thermally activated serpentine: From single- to double-step carbonation<sup>†</sup>

Mischa Werner, Subrahmaniam Hariharan, and Marco Mazzotti\*

Received Xth XXXXXXXXXXXX 20XX, Accepted Xth XXXXXXXXXXXX 20XX

First published on the web Xth XXXXXXXXXXXX 200X

DOI: 10.1039/b000000x

Carbon dioxide capture and utilization by mineralization seeks at combining greenhouse gas emission control with the production of value-added materials in the form of solid carbonates. This experimental work demonstrates that the world's most abundant mineralization precursor, the magnesium (Mg) silicate serpentine, in its thermally activated, partially dehydroxylated form can be carbonated without the use of chemical additives at process temperatures ( $T$ ) below 90 °C and CO<sub>2</sub> partial pressures ( $p\text{CO}_2$ ) below 1 bar. A first series of single-step batch experiments was performed varying the temperature and slurry density to systematically assess the precipitation regime of the relevant Mg-carbonates and the fate of silicon (Si) species in solution. The results suggested that the reaction progress was hindered by a passivating layer of re-precipitated silica or quartz, as well as by equilibrium limitations. Concurrent grinding proved effective in tackling the former problem. A double-step strategy proved successful in addressing the latter problem by controlling the solution pH. This is achieved by continuously removing the Mg from the dissolution reactor and letting it precipitate at higher  $T$  and lower  $p\text{CO}_2$  in a separate reactor, thus yielding a combined  $T$ - $p\text{CO}_2$ -swing — the working principle of a new flue gas mineralization route that is presented herein. Simulations and experiments of the different individual steps of the process are reported, in order to make an assessment of its feasibility.

## 1 Introduction

Understanding the greenhouse gas carbon dioxide (CO<sub>2</sub>) as a recyclable building block for the production of new materials is the big advantage of the CO<sub>2</sub> capture and utilization (CCU) value chain over that based on CO<sub>2</sub> capture and storage (CCS).<sup>1,2</sup> However, most CCU products lack the element of storage, owing to their short life time (e.g. synthetic fuels, fertilizers, etc.). In the case of CCS, the CO<sub>2</sub> is to be disposed off in the subsurface. While being an effective storage strategy, finding public support for this operation has proven to be cumbersome in most parts of the world. Ideally, the utilization of CO<sub>2</sub> would result in its fixation over timescales long enough for true climate change mitigation. To this end, CO<sub>2</sub> can be mineralized in an engineered environment via the extraction of magnesium (Mg) or calcium (Ca) from a suitable precursor material in an aqueous medium, followed by the reaction of these metals with dissolved CO<sub>2</sub> to form carbonates.<sup>3</sup> Converted into a solid, the CO<sub>2</sub> is permanently fixed and the carbonates can be used as raw materials in the con-

struction industry (e.g. for aggregates, dykes, land expansion, etc.) or, from a storage point of view less preferably, in the chemical industry (e.g. as fillers, fire retardants, etc.).<sup>4,5</sup>

Traditionally, the mineralization technology was studied at high temperature with the acidifying help of high CO<sub>2</sub> partial pressures to accelerate the overall rate limiting step, namely the dissolution of the feed material.<sup>6–8</sup> Such operating conditions entail substantial cost related to the need for a separate capture step, as well as to the heat and power requirements of the mineralization plant. Hence, recent developments have seen process concepts that accept dilute CO<sub>2</sub> streams as input.<sup>9</sup> Such concepts often foresee the use of chemical additives that require full recovery.<sup>10,11</sup> However, the cost saved by avoiding a preliminary capture step could also allow for an intensification of the feed pretreatment to counteract the slow dissolution kinetics, while still reducing the overall cost compared to the traditional mineralization scheme.

For serpentine minerals (e.g. lizardite, Mg<sub>3</sub>Si<sub>2</sub>O<sub>5</sub>(OH)<sub>4</sub>), the world's most abundant resource for magnesium and hence the precursor material of choice in this study, an intensified pretreatment refers to thermal activation above ~ 600 °C. At these temperatures, chemically bound hydroxyls (OH) are expelled, thus distorting the mineral's crystal structure and enhancing its reactive surface. O'Connor and coworkers, the group pioneering research on CO<sub>2</sub> mineralization, have used a rather questionable activation strategy to estimate the energy requirements of this activation strategy.<sup>12,13</sup> Consequently, they dis-

<sup>†</sup> Electronic Supplementary Information (ESI) available: [Appendix A - TGA analysis; Appendix B - XRD, SEM, EDX analyses for single-step carbonation product; ; Appendix C - XRD and SEM analysis for double-step carbonation product; Supplementary figures: transformation in the MgO–CO<sub>2</sub>–H<sub>2</sub>O system, complete pH profiles]. See DOI: 10.1039/b000000x/ETH Zurich, Institute of Process Engineering, Sonneggstrasse 3, CH-8092 Zurich, Switzerland. Fax: +4144 6321 141; Tel: +4144 6322 456; E-mail: marco.mazzotti@ipe.mavt.ethz.ch

missed thermal pretreatment as a feasible option to enhance the carbonation efficiency of natural minerals.

### 1.1 Flue gas mineralization studies on activated serpentine

Researchers at Shell Global Solutions International (SGSI) in Amsterdam, NL, were the first to re-consider thermal activation of serpentines as an option for a mineralization process with capture integration.<sup>14,15</sup> Their approach as presented in Verduyn *et al.*<sup>16</sup> involved a Mg-extraction and CO<sub>2</sub> absorption step at moderate temperature and atmospheric pressure, followed by a precipitation step at high temperature and possibly total pressure levels up to 20 bar. After 2009, such research program was continued as a cooperation between SGSI and our group, and then by our group alone.

Balucan *et al.*<sup>17</sup> presented a possible carbonation pathway where flue gas is contacted for several hours with a slurry of activated serpentine in large mineralization ponds. So far, this group has focused mainly on the optimization of the thermal pretreatment process, showing that the activation energy for lizardite can plausibly be reduced to 0.57 GJ t<sup>-1</sup> of ore when applying a more practical heating strategy.<sup>17–19</sup> Only one study was dedicated to the dissolution of activated antigorite using 0.1 M formic acid, yielding a maximum Mg-extraction efficiency of 66 % at 85 °C within 3 h.<sup>20</sup>

Another Australia based group has looked into the kinetics of serpentine dehydroxylation,<sup>21</sup> but are now studying the use of tertiary amines as a regenerable buffer for a two-stage pH-swing process that starts from non-activated serpentine to mineralize flue gas CO<sub>2</sub>.<sup>22</sup> Li *et al.*<sup>23</sup> proposed the use of both an electrochemical and a thermal pretreatment step to realize flue gas CO<sub>2</sub> mineralization via a pH-swing involving sodium and chloride. However, the high energy demand in the form of electric power was soon — and quite rightly so — called into question.<sup>24</sup>

Very recently, a Canadian group has reported dissolution experiments conducted on serpentine mine tailings thermally activated at 650 °C.<sup>25</sup> These authors picked up the aforementioned simple concept of extracting Mg at low temperature under flue gas atmosphere and precipitating Mg-carbonates at higher temperature, originally proposed by SGSI. Pasquier *et al.*<sup>25</sup> reported the release of Mg up to partial pressure levels of  $p\text{CO}_2 = 7.8$  bar at ambient temperature, but did not show the extraction efficiency. For one dissolution experiment, the reactor solution was heated to 40 °C, causing 63 % of the Mg to precipitate in the form of nesquehonite within 3 h. The paper cites two further publications of the same group that should shed light on this preliminary data, but they do not appear to be available yet.

In our group, we investigated the far-from-equilibrium dissolution kinetics of partially dehydroxylated lizardite (hereafter

PDL) at moderate temperatures (up to 120 °C) and low CO<sub>2</sub> partial pressures (up to 2 bar), in order to understand better the physical morphology and chemical properties of the activated material.<sup>26,27</sup> Dissolution efficiencies of up to 83 % at  $p\text{CO}_2 = 1$  bar within 100 min and the prospect of exploiting different  $T$ -levels to maximize the extent of dissolution were among the encouraging results.

Building on the latter, the focus of the present study was set to the investigation of the carbonation potential of PDL under flue gas conditions. First, we report and discuss single-step batch experiments that were performed to gain insight into the precipitation regime of the PDL–CO<sub>2</sub>–H<sub>2</sub>O system. Then we discuss possible improvements to single-step carbonation, including experiments with concurrent grinding and the a novel double-step process driven by the combination of a temperature swing with a CO<sub>2</sub> pressure swing. Simulations and experiments were performed to assess the feasibility of the essential elements of the double-step process. Finally, we conclude in the light of the factors that potentially limit the carbonation efficiency and discuss implications of our findings for the envisioned PDL-based direct flue gas mineralization process.

## 2 Experimental

### 2.1 Materials

Thermally activated lizardite was obtained from SGSI in the form of particles of size under 125 μm with a declared amount of residual OH of 25 mol %. The chemical formula of this partially dehydroxylated material was determined as Mg<sub>2.58</sub>Fe<sub>0.31</sub>Al<sub>0.1</sub>Si<sub>1.87</sub>O<sub>6.5</sub>(OH) (23.95 % wt. Mg), with molar mass of 259 g mol<sup>-1</sup>, and bulk density of 2.69 × 10<sup>3</sup> kg m<sup>-3</sup>. Further details on the characterization of the PDL are reported elsewhere<sup>26</sup>. Selected experiments were performed with a dry-sieved particle size fraction of size under 20 μm. To control the  $p\text{CO}_2$  at ambient pressure, either pure CO<sub>2</sub> (grade 4.5), N<sub>2</sub> (grade 5), or a calibrated gas mixture (±2 % relative error) of 10 % mol. CO<sub>2</sub> in N<sub>2</sub> of the same purity were used (Pangas AG, Switzerland). The starting solution for all experiments consisted in ultrapure de-ionized water (Millipore, 18.2 MΩ cm).

### 2.2 Experimental setups

Most of the experiments reported in this paper were performed on an EasyMax<sup>TM</sup> synthesis workstation (Mettler Toledo, Switzerland) using 100 mL Teflon reactors to limit solute-wall interactions. The reactor lids host a 4-bladed upward stirrer suspended concentrically from the top, as well as ports for temperature sensors, gas dip tubes, reflux-condensers, pH probes, and extra ports that serve to load the PDL at the start of an experiment, to take product slurry samples, to load seeds,

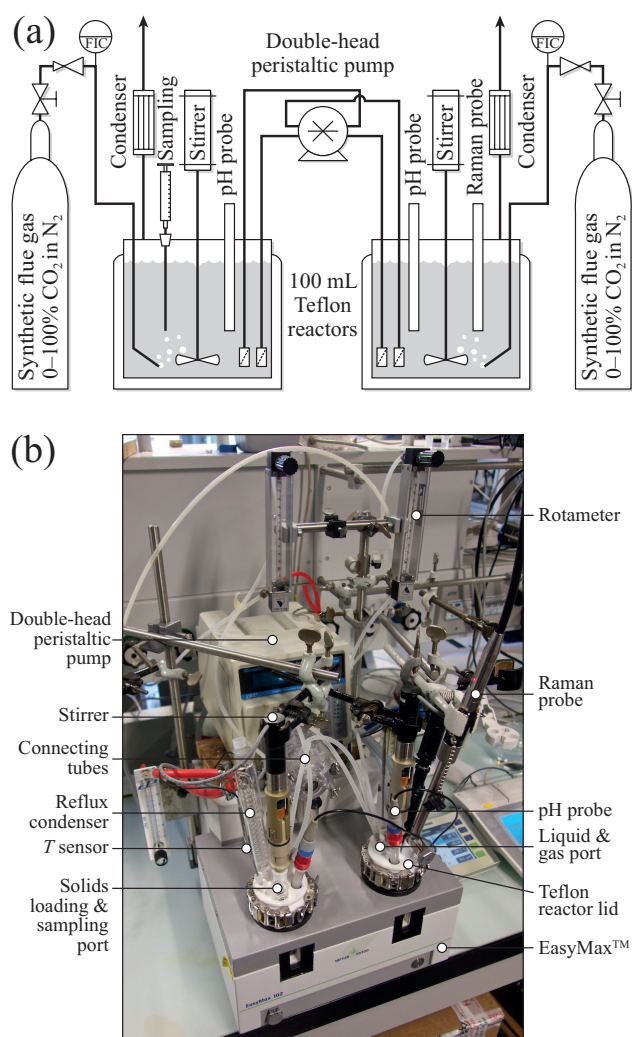


**Fig. 1** (a) Schematic and (b) photograph of the EasyMax™ carbonation setup with annotations.

or to host a Raman probe for the monitoring of precipitating species. The gas supply rate was controlled via rotameters. Fig. 1 shows a schematic of the setup and an annotated photograph of the workstation with both reactors and all peripheral equipment in place.

An extra series of single-step experiments was performed using a rotator ball mill (MiniCer, Netzsch) to study the effect of concurrent grinding on the carbonation efficiency. The drum of the mill has an empty volume of 240 mL and is equipped with an outlet via a rigid disc filter in its center and with an inlet on its top. They are usually used to continuously withdraw and re-inject a slurry stream by means of a peristaltic pump for the purpose of sampling or controlling the slurry temperature and its exposure to a gaseous reactant in a separate reactor. Experiments with such a slurry loop in place were performed,

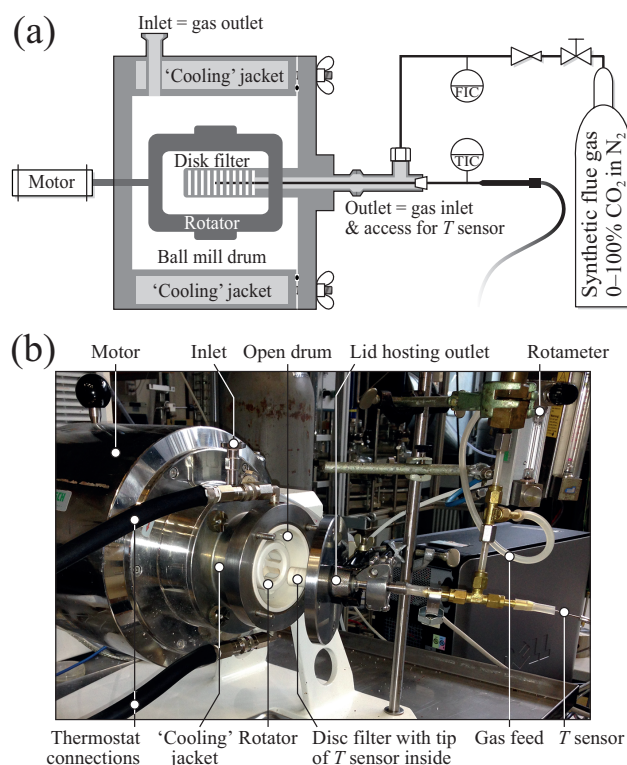


**Fig. 2** (a) Schematic and (b) photograph of the rotator ball mill setup with annotations.

but experimental difficulties were encountered that demanded a change in the setup and protocol (for the interested reader, these experiments and related difficulties are reported elsewhere<sup>28</sup>). As illustrated in Fig. 2, we modified the drum outlet to host a gas inlet and a temperature sensor, the former to introduce gas at controlled flow rate and the latter to control the temperature inside the drum by connecting a thermostat to its cooling jacket. The gas is well dispersed by the rotator and can leave the drum via the open inlet. These changes allowed us to perform carbonation experiments using the drum as a 'reactor' with a controlled temperature and gas atmosphere. To experimentally investigate double-step carbonation, two Teflon reactors were interconnected with two rubber hoses to enable the transport of liquid from one vessel to the other. Two additional dip tubes per reactor realized an inlet and an outlet for the solution. The hoses were installed into the channels of a double-head peristaltic pump in such a way that it is possible to pump the solution from the left to the right reactor and vice versa at the same time (*cf.* Fig. 1). 10  $\mu\text{m}$  solvent filters made of UHMW polyethylene were attached to the dip tubes to avoid transport of solids across the reactors. A Labview™ routine was employed to control the speed and rotational direction of the pump head.

## 2.3 Methods and analytics

**2.3.1 Single-step batch experiments.** Single-step carbonation experiments were carried out in a Teflon reactor at 30, 50, 60, and 90 °C, and at ambient pressure. At each temperature, four different slurry densities or solid to liquid,  $S/L$ , ratios were tested, namely 5, 10, 15, and 20 % wt.. Pure  $\text{CO}_2$  was used as feed gas, bubbled through the reactor at a constant flow rate of  $50 \text{ mL min}^{-1}$ . The runtime was 480 min, during which a total of eight slurry samples of about  $\sim 3 \text{ mL}$  were taken by means of a syringe after 30, 60, 90, 120, 180, 240, 360, and 480 min. To ensure a constant withdrawal position, the tip of the syringe was connected to a rigid dip-tube that can be mounted onto the sampling port.

For each experiment, the reactor was filled with 70 mL of water, the gas flow was established, and stirring was set to 600 rpm, corresponding to the minimum speed to keep particles of size up to  $125 \mu\text{m}$  suspended (tested at 1 % and 20 % wt. slurry density). The reactor temperature, gas-liquid transfer, and  $\text{CO}_2$  speciation were allowed to equilibrate during 30 min, before the addition of the specified amount of PDL marked the start of the experiment. The pH was monitored using a heavy duty probe suitable for suspensions (HA405-DXK, Mettler Toledo), whereas Raman spectra were recorded during selected runs using an immersion probe with a 6 mm spherical lens for enhanced detectability of the precipitates (BallProbe, MarqMetrix, with RXN1 Analyzer, Kaiser Optical Systems, 400 mW laser at 785 nm, 1 min sampling interval, averaged over 3 scans of 15 s exposure). Slurry samples were weighed and quickly filtered through  $0.45 \mu\text{m}$  cellulose nitrate filters. The solids collected were washed and dried at 40 °C under vacuum overnight. Right after taking the last sample, the experiments were stopped, and the same procedure as for the samples was applied to the reactor content.

The liquor collected from the samples was diluted by a factor 120–500 for Mg-analysis and by a factor 100–200 for Si-analysis, depending on the experimental conditions. For iron (Fe) analysis, 1 mL of sample was acidified with 1 mL of 5 M sulfuric acid and then brought to  $\text{pH} > 1$  by adding 1 mL of 5 M NaOH solution. Diluted samples were analyzed using an ion chromatography system (ICS2000, Dionex, CS12A column) to determine the Mg-concentration, while the Si- and Fe-concentration were measured photospectrometrically, as reported elsewhere.<sup>26</sup> The dried solid product was characterized by X-ray diffraction analysis (XRD; LEO 1530, Zeiss  $\text{CuK}\alpha_1$  radiation at  $\lambda = 1.5406 \text{ \AA}$ ) and scanning electron microscopy (SEM; S-4800, Hitachi), partly in combination with energy dispersive X-ray spectroscopy (EDX). Thermogravimetric analysis (TGA; TGA/SDTA851, Mettler Toledo) was performed to determine the extent of carbonation. The amount of TGA sample (150 mg), the temperature ramp (40–900 °C), the heating rate ( $10 \text{ }^\circ\text{C min}^{-1}$ ), and the gas atmosphere in the

furnace ( $\text{N}_2$  at  $50 \text{ mL min}^{-1}$ ) were kept constant.

Important for the interpretation of the measured TGA profiles, either a hydrated or a basic-hydrated Mg-carbonate could be expected in the final product under the experimental conditions applied in this study. Despite being thermodynamically less stable than the anhydrous form magnesite ( $\text{MgCO}_3$ ), numerous studies have confirmed that nesquehonite ( $\text{MgCO}_3 \cdot 3 \text{ H}_2\text{O}$ ) precipitates first at lean  $p\text{CO}_2$  and temperatures below  $\sim 50 \text{ }^\circ\text{C}$ . Instead, higher temperatures and alkaline conditions favor the formation of hydromagnesite ( $(\text{MgCO}_3)_4 \cdot \text{Mg}(\text{OH})_2 \cdot 4 \text{ H}_2\text{O}$ ) (see Hänchen *et al.*<sup>29</sup> and references therein). It was also found that at  $\text{pH} < 9$  nesquehonite can precipitate at temperatures even higher than  $60 \text{ }^\circ\text{C}$ .<sup>30</sup> Following the Ostwald rule of stages, nesquehonite transforms into hydromagnesite, thereby going through a number of intermediates of formula  $(\text{MgCO}_3)_4 \cdot \text{Mg}(\text{OH})_2 \cdot z \text{ H}_2\text{O}$ , with  $4 < z \leq 11$ , if exposed to temperatures higher than  $\sim 50 \text{ }^\circ\text{C}$  (see Fig. S1<sup>†</sup> for an experimental confirmation).<sup>31–34</sup>

During TGA, both nesquehonite and the basic-hydrated Mg-carbonates decarbonate between  $\sim 300 \text{ }^\circ\text{C}$  and  $550 \text{ }^\circ\text{C}$ , while dehydration and dehydroxylation occurs at lower temperature.<sup>31,35–38</sup> In our TGA profiles, the absence or presence of a dehydroxylation step, *i.e.* a drop in mass between  $\sim 200 \text{ }^\circ\text{C}$  and  $300 \text{ }^\circ\text{C}$ , rendered it possible to identify the carbonate in the sample either as nesquehonite or as a basic-hydrated Mg-carbonate, respectively. Additional total inorganic carbon content analysis on selected samples allowed to delimit the exact temperature window to be considered for determining the mass fraction of  $\text{CO}_2$ ,  $x_{\text{CO}_2}$ , from the TGA profiles (Appendix A<sup>†</sup>). Knowing  $x_{\text{CO}_2}$  and the mass fraction of Mg in the unreacted PDL,  $x_{\text{Mg},0}$ , the extent of carbonation of the samples,  $R_x$ , was calculated as

$$R_x = \frac{x_{\text{CO}_2} M_{\text{Mg}}}{(1 - x_{\text{CO}_2} + C) x_{\text{Mg},0} M_{\text{CO}_2}}, \quad (1)$$

where  $M_{\text{Mg}}$  and  $M_{\text{CO}_2}$  are the molar masses of Mg and  $\text{CO}_2$ , respectively. The denominator in the first quotient of Eq. (1) corrects for the weight increase by the mineralized  $\text{CO}_2$ , while the parameter  $C$  lumps corrections for the mass of the aqueous Mg and Si present in the sample liquor, as well as for the removal of the residual hydroxyl from the PDL upon carbonation (see Appendix A<sup>†</sup> for the derivation).

Based on the amount of liquor sampled and collected, as well as on the Mg-concentration therein, the accumulation of moles of Mg in the reactor solution between samples  $i - 1$  and  $i$ ,  $\Delta n_{\text{Mg},i}$  ( $i = 1, \dots, 8$ ) was determined. The accumulation of moles of Mg in the solid product between two samples was obtained from the change in the extent of carbonation,  $\Delta R_{x,i}$ , and the initial amount of Mg in the solid feed,  $n_{\text{Mg},0}$ . Hence, the extent of dissolution with respect to Mg at the end of each

sampling interval,  $X_{\text{Mg},i}$ , is given by

$$X_{\text{Mg},i} = \frac{\sum_{k=1}^i \Delta n_{\text{Mg},1,k} + r n_{\text{Mg},0} \sum_{k=1}^i \Delta R_{x,k}}{n_{\text{Mg},0}}, \quad (2)$$

where the parameter  $r$  corresponds to the Mg:CO<sub>2</sub> ratio of the relevant Mg-carbonate ( $r = 1$  for nesquehonite,  $r = 5/4$  for the basic-hydrated Mg-carbonate).

**2.3.2 Experiments with concurrent grinding.** Experiments in the ball mill drum were performed at 30 and 50 °C, at atmospheric pressure under continuous gas flow of pure CO<sub>2</sub> at 10 mL min<sup>-1</sup>, using slurry densities of 10 % wt. and 20 % wt., and for total runtimes of 60, 120, and 240 min. For each experiment, 90 mL or 80 mL of water was filled into the drum through its inlet. After establishing the gas flow, the rotator speed was set to 600 rpm to equilibrate CO<sub>2</sub> speciation and temperature for 30 min. Then, the mill was stopped and the PDL together with 340 g of zirconium beads of 1.5 mm diameter (occupying a volume of 60 mL) were added through the inlet. The re-start of the mill marked the start of an experiment. At the end, the content in the drum was passed through a 630 μm lab sieve. The handling of the solid product upon filtration followed the same procedure as described above.

**2.3.3 Double-step experiments.** Double-step carbonation experiments were carried out at atmospheric pressure using one of the interconnected Teflon reactors as the precipitator, and the other one as the dissolution reactor. The runtime (240 min), the CO<sub>2</sub> content of the feed gas (100 %), and the slurry density (1 % wt.) in the dissolution reactor, as well as the temperature in the precipitator (90 °C) were kept unchanged. Variations in temperature and particle size of the PDL used in the dissolution reactor, as well as of the CO<sub>2</sub> content in the feed gas and the amount of seeds used in the precipitator are reported together with the experimental results in Table 1.

For each experiment, the dissolution reactor and precipitator were filled with 99 mL and 80 mL of water, respectively. Also the two connectors between the reactors were filled with water (6.8 mL each, incl. the dead-volume of the filters), before closing them with the pH probes in place and the Raman probe installed in the precipitator. Then, the gas flow was established at 50 mL min<sup>-1</sup> and the temperature and CO<sub>2</sub> speciation were allowed to equilibrate for 60 min. After 45 min, the peristaltic pump was started at a rate of 10 mL min<sup>-1</sup>, yielding a mean residence time of the liquid inside the reactors of roughly 30 min. The addition of the PDL into the dissolution reactor marked the start of an experiment. For most of the experiments, a designated amount of seeds was added to the precipitator 9 min after the start, when the transfer of Mg from the dissolution reactor has already increased the pH inside the precipitator to pH > 7.8. The seeds have been taken from the product that precipitated during an unseeded test experiment.

Throughout the runtime, the rotational direction of the peristaltic pump was reversed automatically after every minute, which effectively prevented the filters from clogging. At the end of the experiments, the lids were opened and the peristaltic pump was switched one last time to reverse flow, thus emptying the solution inside the connectors back into the reactors. The content in both reactors was handled in the same way as described for the single-step experiments. For the Mg- and Si-concentration analysis, dilutions (factor ~ 120) from the collected liquor were performed in triplicates. The extent of dissolution with respect to Mg was calculated based on the mass,  $m_l$ , and Mg-concentration,  $c_{\text{Mg}}$ , of the liquor in both reactors (diss. and prec.), together with the mass,  $m_s$  (corrected for the mass of seeds,  $m_{\text{seed}}$ ), and molar weight,  $M_s$ , of the final solid product in the precipitator:

$$X_{\text{Mg}} = \frac{m_l^{\text{diss.}} c_{\text{Mg}}^{\text{diss.}} + m_l^{\text{prec.}} c_{\text{Mg}}^{\text{prec.}} + 5(m_s^{\text{prec.}} - m_{\text{seed}})/M_s}{n_{\text{Mg},0}}. \quad (3)$$

The moles of Mg in the solid product over  $n_{\text{Mg},0}$  in Eq. 3 yields the extent of carbonation,  $R_x$ . Based on our knowledge from the characterization of the high- $T$  solid product by XRD (Appendices B and C<sup>†</sup>), we assumed the chemical composition of the basic-hydrated Mg-carbonate that formed in our experiments to be best comparable to the one of dypingite ((MgCO<sub>3</sub>)<sub>4</sub>·Mg(OH)<sub>2</sub>·4H<sub>2</sub>O,  $M_s = 486$  g mol<sup>-1</sup>).

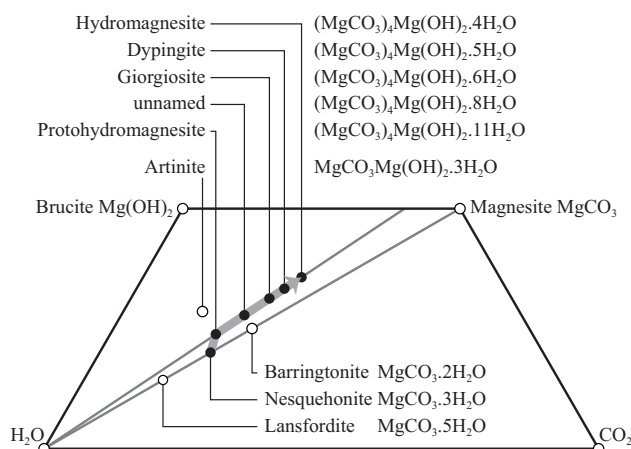


**Fig. 3** Position of the hydrated and basic-hydrated Mg-carbonates in the lower half of the ternary phase diagram for the MgO–CO<sub>2</sub>–H<sub>2</sub>O system (adapted from Hopkinson *et al.*<sup>33</sup>). The gray arrow represents the transformation sequence from nesquehonite to hydromagnesite.

**2.3.4 Solubility calculations.** The geochemical equilibrium software package EQ3/6 and a database employing the B-Dot activity coefficient model (*ymp*-database)<sup>39</sup> was used

to calculate the solubilities of nesquehonite and hydromagnesite, as well as those of amorphous silica and quartz ( $\text{SiO}_2$ ) at the conditions relevant for this study. Given that silicic acid with a  $pK_a = 9.84$  does not dissociate to any significant extent under the conditions studied, only the operating temperature and  $\text{CO}_2$  fugacity were used as inputs. The  $\text{CO}_2$  fugacity was calculated following the methodology reported elsewhere.<sup>26</sup> As aforementioned, literature provides evidence for several intermediates that can be found in the  $\text{MgO}-\text{CO}_2-\text{H}_2\text{O}$  system during the transition from nesquehonite to hydromagnesite (Fig. 3). Owing to their metastable nature, there are no thermodynamic data available. However, one can reasonably conjecture that their solubilities lie in between those of the two end-members, namely nesquehonite and hydromagnesite, *i.e.* those that we calculated. Note also that these calculations are only indicative for the experimental reality, since they assume perfect equilibrium, while our system was constantly subject to changing conditions due to Mg-extraction, make-up of  $\text{CO}_2$  dissolution, and precipitation of carbonates. Moreover, although contained only in small quantities in the unreacted PDL, impurities like iron or calcium that are released into and/or removed from the solution at their own rate may have an influence on the apparent solubilities. For these reasons, the calculated solubility data used in the discussion hereafter provide an indication of the relevant concentration domain and should not be used to pinpoint the exact distance from thermodynamic equilibrium.

### 3 Single-step carbonation

Systematically changing the temperature and the slurry density in batch mode should give a first appraisal of the carbonation performance of partially dehydroxylated lizardite under realistic process conditions. Out of the 16 combinations of operating parameters that were tested, the experiment at  $30^\circ\text{C}$  and 20% wt. slurry density was repeated three times in order to check for the reproducibility of experimental protocols and analytical methods. The outcome is illustrated in Fig. 4, which shows the entire set of data collected during the experiments, *i.e.* the Mg-concentration and the pH, the Si- and Fe-concentration, as well as the extent of carbonation and dissolution,  $R_x$  and  $X_{\text{Mg}}$ , respectively. All measurements for the three replicates show an excellent match.

Hereafter, we first describe the phenomenology of the replicated reference experiment in more detail, before we report the effect of temperature exemplarily for the four experiments at 20% wt. slurry density. Then, the effect of the slurry density is reported by showing the complete set of carbonation experiments performed in single-step mode.

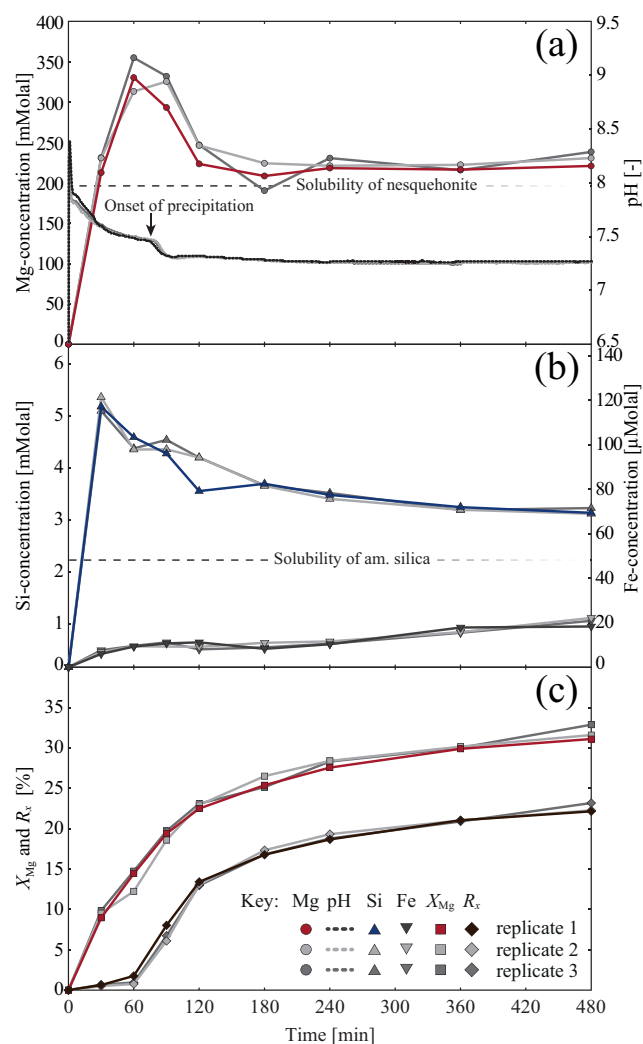


**Fig. 4** Single-step carbonation at  $30^\circ\text{C}$  and  $S/L = 20\%$  wt.: three replicates of (a) the Mg-concentration ( $\circ$ ) and pH (dotted lines), (b) the Si- ( $\Delta$ ) and Fe-concentration ( $\nabla$ ), and (c) the extent of carbonation  $R_x$  ( $\diamond$ ) and dissolution  $X_{\text{Mg}}$  ( $\square$ ). The pH in (a) starts at a lower value than shown in the figure ( $\text{pH}(t=0) \approx 4$ ). The Mg- and Si-concentration corresponding to nesquehonite and amorphous silica, respectively, are indicated in (a) and (b) as dashed lines.

#### 3.1 Phenomenology of the reference experiment

As follows from Fig. 4a, upon addition of the PDL, the pH increased rapidly from  $\text{pH}(t=0) \approx 4$  (out of range in Fig. 4a) to a peak level close to 8.5, due to the initially fast extraction of Mg via proton exchange. The alkaline solution was able to take up more  $\text{CO}_2$ , causing the pH to decrease gradually thereafter. The onset of precipitation is manifested by a sudden drop in pH after  $\sim 75$  min. Note that the Mg-concentration exceeded the calculated solubility of nesquehonite by over

70 % before the rate of Mg-release was overtaken by the rate of Mg-consumption via precipitation. Thereafter, the Mg-concentration remained close to the solubility line, and the pH stabilized at a correspondingly high level of  $\sim 7.3$ .

Much less Si was measured in solution than expected from our dissolution model valid at far-from-equilibrium conditions, *i.e.* for dissolution experiments at extremely low solid to liquid,  $S/L$ , ratios.<sup>27</sup> Also there, dissolution was understoichiometric with respect to Si, an evidence that we conceptualized in the light of three effects reported in literature, namely the formation of a Si-rich leached layer, the re-polymerization of silanol groups therein, and the presence of multiple dissolving species in partially dehydroxylated lizardite.<sup>26</sup> Following from Fig. 4b, the Si-concentration in this experiment exceeded the calculated solubility of amorphous silica by at least a factor two but then slowly approached this solubility line without reaching it during the course of the experiment. This trend adds another element of complexity, as it shows clearly that at high slurry densities, Si is bound to form a solid via a dissolution/re-precipitation mechanism.

The low concentration levels of iron indicate that our activated lizardite contains this element in a barely soluble form (see also elsewhere<sup>26</sup>), which suggests its influence on the carbonation efficiency to be minor and not worth discussing.

In agreement with the observed dynamics of the pH and Mg-concentration profiles, the extent of carbonation measured in the sampled solids started to increase between 60 and 90 min. However, after  $\sim 120$  min the sharp initial increase was followed by a strikingly reduced increase during the remaining runtime, leading to a final carbonation efficiency of  $R_x \approx 20\%$ . The same two stage dynamics can be observed for the extent of dissolution with respect to Mg, the latter reaching a level of  $X_{\text{Mg}} \approx 30\%$  by the end of the experiment.

### 3.2 Effect of temperature

The effect of temperature is shown in Fig. 5 for the highest slurry density investigated (20 % wt.). The measured Mg- and Si-concentration profiles are plotted next to the solubility lines calculated as a function of  $T$ . The final Mg-concentration levels in Fig. 5a show a substantial decrease with  $T$ . Indeed, as follows from Fig. 5e the calculated solubility of nesquehonite, which is expected to govern precipitation at 30 °C and 50 °C, is substantially higher ( $\sim 150$ – $200$  mMolal for  $T \leq 50$  °C) than that of hydromagnesite ( $< 30$  mMolal for  $T \geq 60$  °C), which can be viewed as the minimal Mg-concentration level attainable in a perfectly equilibrated system at 60 °C and 90 °C.

The Si-concentration profiles in Fig. 5b showed a small increase with  $T$  up to 60 °C, but then dropped to a much lower level for the experiment at 90 °C, where the final Si-concentration in the reactor was in good agreement with the theoretical solubility of quartz (Fig. 5f). Instead, the final Si-

concentration at 50 and 60 °C were very close to the solubility of amorphous silica. At 30 °C, the Si-concentration was constantly above the latter solubility, as described in Subsection 3.1. Apparently, in accordance with the empirical observation summarized in the Ostwald rule of stages, also in the case of Si there is a change from the precipitation of a more soluble compound (amorphous silica) forming at lower  $T$  to the direct precipitation of the less soluble but thermodynamically more stable compound (quartz) at high  $T$ . In the former case, amorphous silica can transform into quartz if the kinetics of this process allows.

The measured pH profiles overlap during most of the experimental runtime, hence an offset relative to the profile at 30 °C is applied for their representation in Fig. 5c. This helps in identifying the previously discussed drop in pH coinciding with the onset of precipitation. Note that at  $T > 30$  °C, the drop was followed by a temporary increase of the pH, possibly because the rate of Mg-extraction profited from the fast shift to slightly less alkaline conditions.

The same two stage dynamics of the extent of carbonation described in Subsection 3.1 is exhibited by the  $R_x$  profiles at the three higher temperatures investigated (Fig. 5d). A level of no more than  $\sim 15\%$  was reached during the more or less steep increase in  $R_x$  after the onset of precipitation. Contrary to the increase in the dissolution efficiency with  $T$  that was measured during our far-from-equilibrium experimental campaign,<sup>26</sup> the final  $R_x$  after the experiments at 60 and 90 °C was lower than after those at 30 and 50 °C.

The variations in the measured level of the Mg-concentration and in the evolution of the  $R_x$  profiles are reflected in the dynamics of the calculated extent of dissolution with respect to Mg (Fig. 5g). The increase in  $X_{\text{Mg}}$  at 60 °C after the sixth sample is due to nesquehonite transforming into a basic-hydrated Mg-carbonate. From test experiments with online Raman monitoring we were aware of this phenomenon taking place at 60 °C, whereas at 90 °C the basic-hydrated Mg-carbonate precipitated without going through a transformation (see Fig. S1a<sup>†</sup>). A number of evidences allowed to determine the time after which transformation occurred: 1) the TGA profiles up to the sixth sample were lacking the mass loss due to dehydroxylation, while this was present in the profiles of the last two samples; 2) during transformation, the Mg-content in the carbonate, but not the carbon content, increases by 25 %; accordingly, the Mg-concentration in the reactor decreased, as can be seen from the drop between the sixth and seventh sample in the corresponding profile in Fig. 5a; 3) this transformation and hence the consumption of Mg from the solution must have taken place over a relatively short period of time, so as one can also observe a drop in the corresponding pH profile, marked in Fig. 5c as the onset of transformation short before  $t = 300$  min; 4) the validity of our interpretation of the TGA, Mg-concentration, and pH profiles was confirmed by

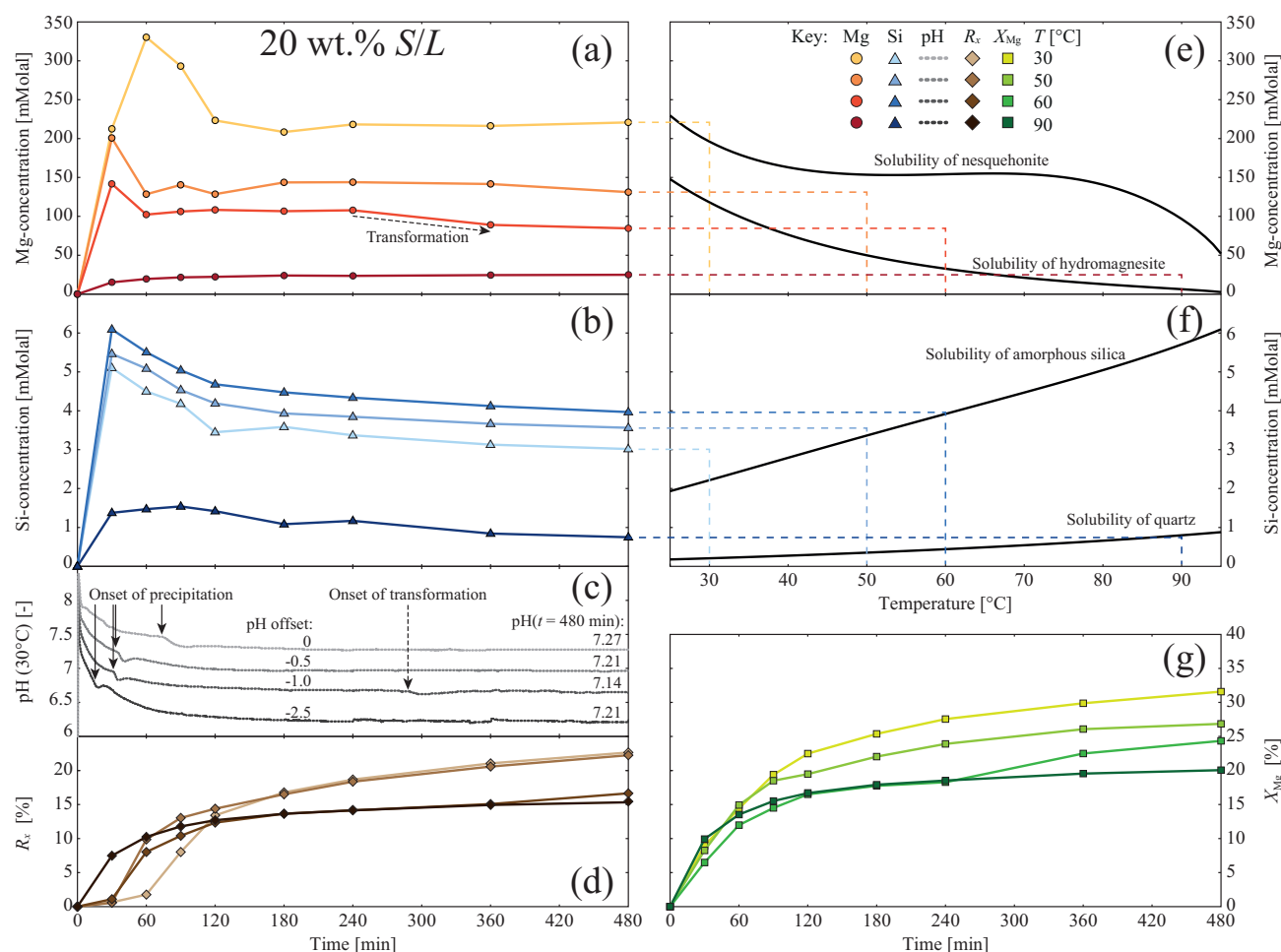


**Fig. 5** Effect of temperature on single-step carbonation: Evolution of (a) the Mg-concentration ( $\circ$ , orange) next to the (e) solubility of nesquehonite and hydromagnesite vs.  $T$ , (b) the Si-concentration ( $\triangle$ , blue) next to the (f) solubility of amorphous silica and quartz versus  $T$ , (c) the reactor pH (dotted lines, gray), (d) the extent of carbonation  $R_x$  ( $\diamond$ , brown), and (g) the extent of dissolution  $X_{Mg}$  ( $\square$ , green) for experiments with  $S/L = 20\%$  wt.. The color intensity indicates the temperature from 30 °C (faint) to 90 °C (intense). The y-axis in (c) is valid for the pH measured at 30 °C, while the other three pH profiles are offset for the sake of better readability. The solid and dashed arrows in (c) indicate the onset of precipitation and transformation, respectively.

the results from additional offline analyses of the solid product (XRD, SEM, EDX; see Appendix B<sup>†</sup>).

### 3.3 Effect of slurry density

The complete set of single-step experiments conducted at 30 °C and 50 °C as well as at 60 °C and 90 °C is illustrated in Fig. 6 and Fig. 7, respectively. Increasing the slurry density from 5 to 20 % wt. reduced the time until the onset of precipitation,  $t_{\text{onset}}$ , most notably at 30 °C. Only the two 5 % wt. at 30 °C and 50 °C did not reach a noticeable onset of precipitation, whereas the formation of Mg-carbonates was observed at all other conditions. The carbonates that

formed during experiments with  $S/L = 5\text{--}15\%$  wt. were identical to the ones identified and described above for the four experiments with  $S/L = 20\%$  wt. — including the fact that the transformation at 60 °C occurred sometime between the sixth and seventh sample.

In those experiments with significant formation of carbonates, the slurry density had little to no effect on the final concentration level of both Mg and Si. After the runtime of 480 min, the solute concentrations appear to have stabilized on a level corresponding to the effective solubility with respect to the mineral phases present in the reactor. Concerning the Mg-carbonates, the effective solubilities at 30 °C (Fig. 6a) were slightly above the calculated solubility

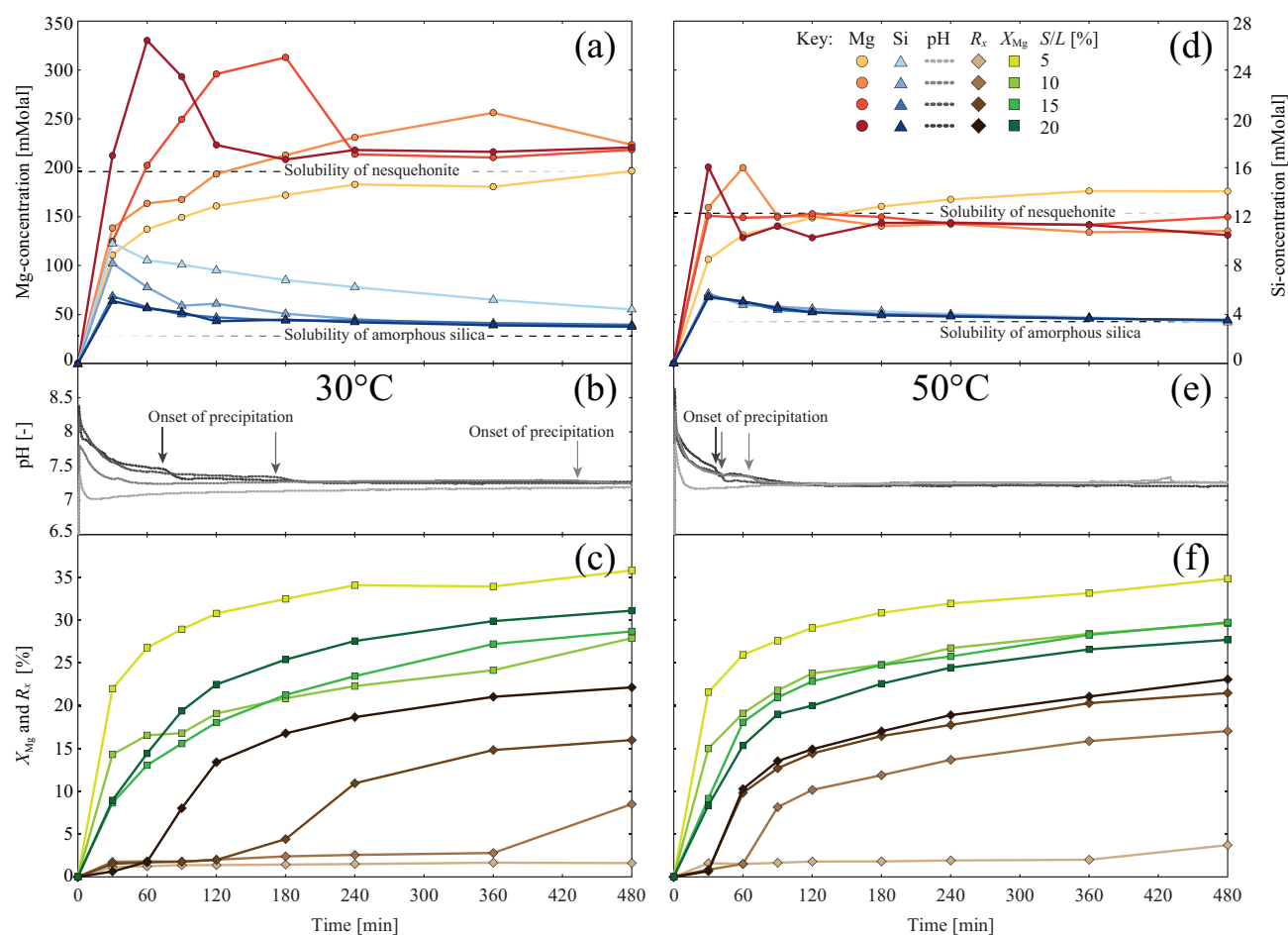


**Fig. 6** Effect of slurry density on single-step carbonation: Evolution of the (a,d) Mg-concentration ( $\circ$ , orange) and Si-concentration ( $\triangle$ , blue), (b,e) reactor pH (dotted line, gray), and (c,f) the extent of dissolution  $X_{Mg}$  ( $\square$ , green) and carbonation  $R_x$  ( $\diamond$ , brown) for experiments at (a-c) 30 °C and (d-f) 50 °C. The color intensity indicates the  $S/L$  ratio from 5 % wt. (faint) to 20 % wt. (intense). The dashed lines in (a,d) correspond to the Mg and Si solubility concentrations for the relevant precipitates. The arrows in (b,e) indicate the onset of precipitation.

of nesquehonite, whereas at 50 °C (Fig. 6d) they were slightly below. At 60 °C (Fig. 7a), neither the seemingly stable level prior to transformation, nor the final level thereafter were anywhere close to the corresponding calculated solubilities of nesquehonite and hydromagnesite. Apparently, the actual driving force for precipitation at this temperature must have been quite different from the ideal system assumed for the solubility calculations (see Subsection 2.3.4 for a detailed discussion about this issue). The discrepancy at the end of the experiment is less surprising, as it was already clear from the XRD analysis that the final product is different from hydromagnesite. Also at 90 °C (Fig. 7d), the measured Mg-concentration levels were overlapping and perfectly flat, but on a level that is four times higher than the calculated hydromagnesite solubility at this  $T$ .

The Si-concentration levels exhibited less discrepancy between the calculated solubilities and the apparent ones. An effect of the slurry density can be observed at 30 °C (Fig. 6a) and at 90 °C (Fig. 7d), namely that the Si-concentrations were closer to the calculated solubility of amorphous silica or quartz, when larger slurry densities were selected. Obviously, re-precipitation was more efficient the more particles were added at  $t = 0$ , *i.e.* the higher the absolute dissolution rate of Si after the start of the experiment. Likely, the rate of re-precipitation overtook the rate of Si-release already within the first 30 min, *i.e.* prior to collecting the first sample. The corresponding maximum concentration level was then the higher and was reached the sooner the higher the slurry density (as can also be observed for the Mg-concentration profiles in Fig. 6a). Hence, more nuclei could form and grow,

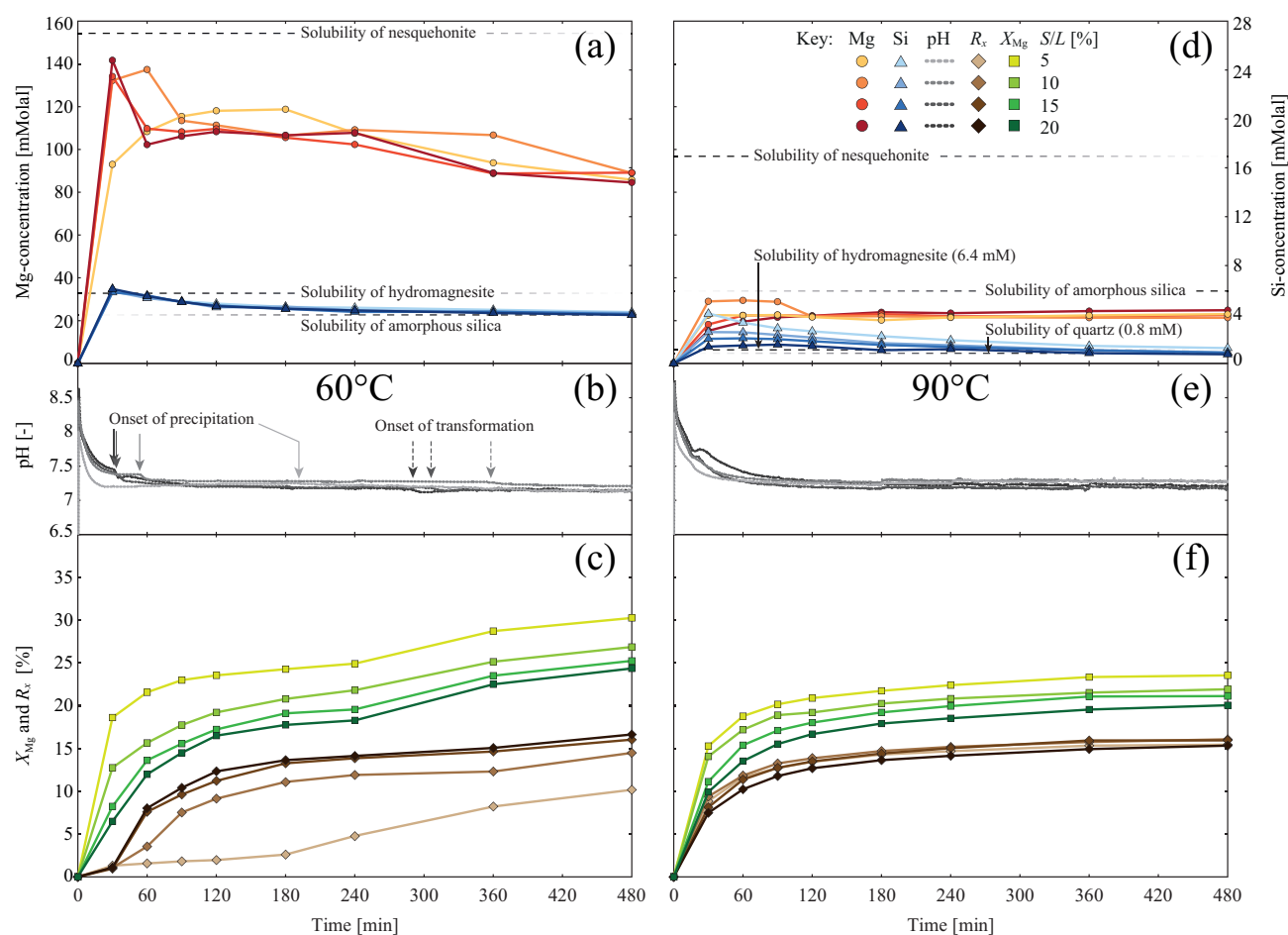


**Fig. 7** Effect of slurry density on single-step carbonation: Evolution of the (a,d) Mg-concentration ( $\circ$ , orange) and Si-concentration ( $\Delta$ , blue), (b,e) reactor pH (dotted line, gray), and (c,f) the extent of dissolution  $X_{Mg}$  ( $\square$ , green) and carbonation  $R_x$  ( $\diamond$ , brown) for experiments at (a-c) 60 °C and (d-f) 90 °C. The color intensity indicates the slurry density from 5 % wt. (faint) to 20 % wt. (intense). Note the difference in scale for the Mg-concentration in (a,c) as compared to the corresponding axis in Fig. 6. The dashed lines in (a,d) correspond to the Mg and Si solubility concentrations for the relevant precipitates. The solid arrows in (b,e) indicate the onset of precipitation, the dashed arrows in (b) indicate the onset of transformation (see text).

thus removing Si from solution more rapidly at the higher slurry densities. At 50 °C and 60 °C (Figs. 6d and 7a) the kinetics of re-precipitation are faster and quartz does not yet form, with the consequence that the slurry density had no influence on the observed Si-concentration level.

The influence of the slurry density on the measured extent of carbonation was largest at 30 °C (Fig. 6c), where a higher slurry density not only reduced  $t_{\text{onset}}$  but also led to higher final  $R_x$  values. This trend faded gradually away at the higher temperatures and slurry densities investigated. Generally, the maximum final carbonation efficiency was measured to be only about 20 % at 30 °C and 50 °C, whereas it was even lower at 60 °C and 90 °C, namely about 15 %.

A lower slurry density led to higher Mg-extraction efficiencies, except for the  $S/L = 10\%$  experiment at 30 °C (Fig. 6c), which reached a lower  $X_{Mg}$  than the experiments with a higher slurry density where precipitation started much earlier. Also the slope of the initially fast increase of  $X_{Mg}$  was steeper the lower the slurry density, which may be explained with the impact of the latter on the pH evolution right after the start. Adding a lower amount of PDL led to lower peak values of the pH and to a faster make-up of acidity by the pickup of  $\text{CO}_2$  dissolution (see Figs. 6b,e and 7b,e). After this fluctuations, the pH leveled out in a range between 7.1 and 7.3 during the remaining part of the experiment, independent of the experimental conditions applied.

## 4 Discussion of single-step carbonation and possible improvements

It is worth comparing the maximum Mg-extraction efficiency attained in the single-step experiments with the extent of dissolution with respect to Mg at far-from-equilibrium conditions that we measured earlier using the same PDL material.<sup>26</sup> When choosing a very small solid to liquid ratio, but applying the same  $p\text{CO}_2$  and temperature, the  $X_{\text{Mg}}$  level after 480 min reached 49.2 % instead of the 36.6 % observed for the  $S/L = 5\%$  wt. experiment at 30 °C in this study, 68.9 % instead of 30.3 % at 60 °C, and 88.8 % instead of 23.5 % at 90 °C.

In response to this striking difference and generally to the low carbonation efficiencies attained in single-step mode, two hypotheses were put forward. First, after the Mg extracted until the onset of precipitation has been more or less quickly consumed by precipitation down to the apparent solubility level, further reaction progress might have been hindered by the formation of a passivating layer on the surface of the dissolving PDL particles. Such a layer could consist either of reprecipitated amorphous silica or quartz, or of Mg-carbonates that precipitated via heterogeneous nucleation — or of a combination of both. Second, the fact that the pH level stabilized at a high level short after  $t_{\text{onset}}$  suggests that by then the available acidity was too low for effective Mg-extraction.

The two hypotheses were used to develop alternatives to single-step carbonation, which are presented in the following. First, the outcome of the experimental campaign with concurrent grinding is reported. Then, we introduce the concept of a double-step process with a thermodynamic driving force arising from the combination of a temperature swing with a  $\text{CO}_2$  pressure swing.

### 4.1 Carbonation with concurrent grinding

The hypothesis of a passivating surface layer was challenged by performing experiments with concurrent grinding, which should help to remove a passivating layer and to create fresh reactive surface. The results from the series at 30 °C and with  $S/L = 10\%$  wt. are shown in Fig. 8a together with the data from the Teflon reactor at equal conditions. Note that values of  $R_x$  obtained in the ball mill drum are connected by a line to guide the eye, although they correspond to independent experiments. A substantial increase of  $R_x$  was measured between the 60 min and 120 min experiment, but no further reaction progress occurred when doubling the runtime to 240 min; the latter runtime was applied twice to confirm reproducibility. The runtime of 120 min served as the reference time, for which additional experiments were performed, namely without the grinding medium in place, at 10 % wt. instead of 20 % wt.

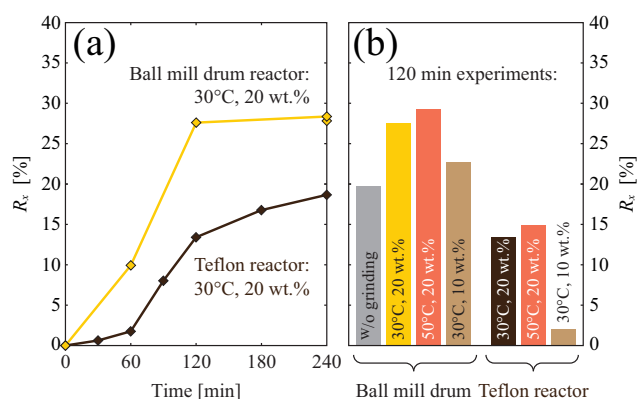


**Fig. 8** Effect of concurrent grinding on the carbonation efficiency in the ball mill drum reactor at (a) 30 °C with  $S/L = 20\%$  wt. and (b) at variations of these conditions as annotated, for experiments lasting 120 min. For comparison, the corresponding experiments in the Teflon reactor are shown, too.

slurry density, and at 50 °C instead of 30 °C. The results can be analyzed and compared in Fig. 8b, where also the corresponding Teflon reactor data is included for comparison. From these results it is evident that the effect of concurrent grinding should rather be appreciated from the difference between the two experiments with and without grinding medium (+7.6 % points) than from the difference between the two reactors apparent in Fig. 8. Going from the Teflon reactor into the ball mill drum already caused a difference in  $R_x$  of +6.1 % points even without adding the grinding medium yet. This could be attributed to particle-particle and particle-wall collisions induced by the bulky rotator of the mill (see Fig. 2). Increasing the temperature to 50 °C had a similarly small effect in the two reactors. Interestingly, a lower slurry density of 10 % wt. reduced  $R_x$  by only  $-4.7\%$  points in the case with concurrent grinding, whereas virtually no carbonation occurred up to 120 min in the corresponding Teflon reactor. In fact, it took more than 420 min in the latter reactor to reach  $t_{\text{onset}}$  (cf. Fig. 6c). Thus, concurrent grinding seems effective to foster Mg-extraction and thereby reducing the time for the onset of precipitation, but based on these few explorative experiments it is not possible to attribute this effect to a specific mechanism. However, with a measured maximum of  $R_x < 30\%$  the overall carbonation efficiency was still quite low.

### 4.2 Combined $T$ -swing and $p\text{CO}_2$ -swing process

The hypothesis that the evolution of the pH during the single-step process is disadvantageous for further Mg-extraction was addressed by spatially decoupling the PDL dissolution from the precipitation reaction. This should also allow for elimi-

nating a potentially passivating effect of the carbonate precipitates on the dissolution efficiency. Most simply, and without the need of pH-tuning agents, two reactors can be operated at different temperature and  $p\text{CO}_2$  to promote Mg-extraction in the dissolution reactor, while enabling precipitation only in the precipitator. Inside the latter, a low  $p\text{CO}_2$  and a high temperature are favorable, as this reduces the proton activity and the solubility of carbonates. On the contrary, an elevated  $p\text{CO}_2$  in the dissolution reactor maximizes the gas-liquid transfer of  $\text{CO}_2$ , thereby reducing the pH and facilitating Mg-extraction. The maximum Mg-concentration in the dissolution reactor is limited by the solubility of the kinetically relevant Mg-carbonate species at the operating conditions applied. Since the solubility of carbonates decreases with temperature, it might be tempting to suggest a low temperature for the dissolution operation. However, our far-from-equilibrium analysis suggests that the dissolution efficiency of the PDL increases with temperature.<sup>26,27</sup> A possible solution is to contact the liquid and solid streams in a counter current operation using two or more dissolution reactors, so as the dissolution temperature for the solid particles increases with time.<sup>26</sup>

A flow scheme including the essential elements of the proposed double-step flue gas mineralization process is presented in Fig. 9a. Coming from the low temperature high  $p\text{CO}_2$  dissolution reactor R1, the liquid stream L1 contains a high amount of dissolved  $\text{CO}_2$ , which partially degases in the high temperature precipitator R3. This excess  $\text{CO}_2$  is carried on by the flue gas that enters the process in R3, thus facilitating the degassing and ensuring the desired low  $p\text{CO}_2$  therein. After precipitation, the  $\text{CO}_2$  and Mg lean liquid stream L2 is pumped into the dissolution reactor R2. The higher temperature therein, the elevated  $p\text{CO}_2$  right after the booster, as well as the low Mg-concentration in L2 help to recover Mg from the partially dissolved PDL, *i.e.* that part that could not be extracted at the low temperature of R1. However, the higher gas solubility at the temperature in R1 enables the solution to take up more  $\text{CO}_2$ , which decreases the pH and facilitates the extraction of the fast dissolving Mg from the incoming fresh PDL. Thus, the solution on the dissolution side of the process becomes gradually enriched with both Mg and  $\text{CO}_2$ , *i.e.* going from R2 to R1.

The underlying driving force of the process can be best explained with the help of the concentration-temperature diagram reported in Fig. 9b, which shows a schematic of the evolution of the Mg-concentration during the different stages of a process cycle. Also plotted are the calculated solubility lines of the two Mg-carbonates that are kinetically relevant at the operating conditions of R1 and R3. Note that the illustrated concentration levels, as well as the  $T$ - and  $p\text{CO}_2$  levels in Fig. 9b are conceptual and should not be interpreted quantitatively ( $p\text{CO}_2$  in R3 corresponds to the  $\text{CO}_2$  content of a typical flue gas, though). In a real process, temperature and

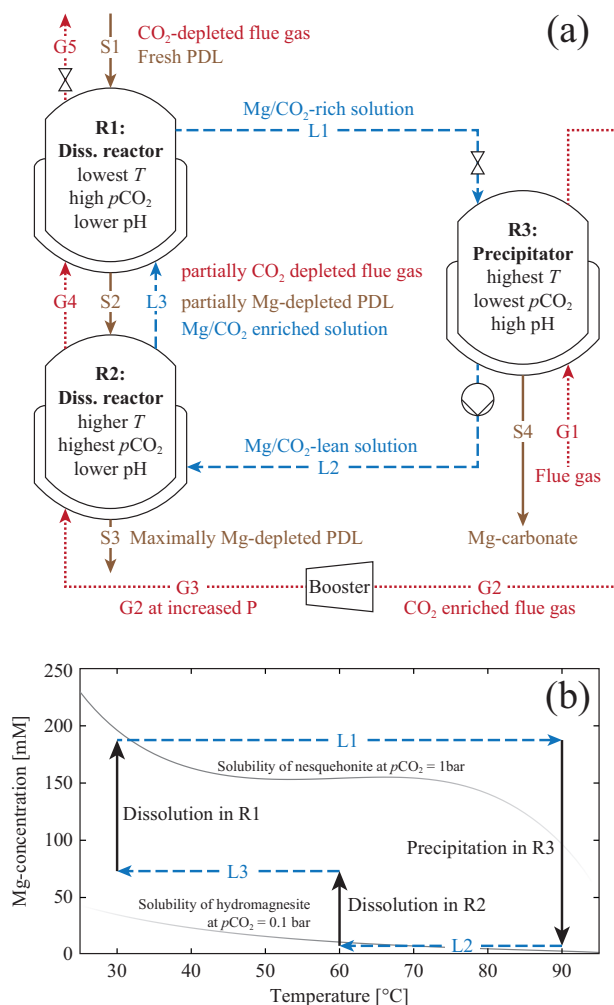


**Fig. 9** (a) Flow scheme of a combined  $T$ - $p\text{CO}_2$ -swing process with two dissolution stages and one precipitator, connected by gas streams (dotted lines, red), liquid streams (dashed lines, blue), and solid streams (solid lines, brown). (b) Concentration-temperature diagram showing conceptually the evolution of the Mg-concentration during the different stages of a process cycle. Dashed arrows correspond to the transport of liquid across the reactors as represented in (a). Grey lines indicate the Mg solubility concentration of the kinetically relevant Mg-carbonates.

pressure would be subject to optimization, together with the variables offering additional degrees of freedom, namely the reactor residence times of the solid, liquid, and gas streams. In the dissolution reactors, the residence times for the various streams will be dictated by the dissolution kinetics of the PDL. In the precipitator, which can be viewed as a mixed-suspension mixed-product removal (MSMPR) crystallizer, long residence times of the liquid would result in a low steady-state concentrations of Mg, so as the effluent would be

Mg-lean as desired. However, effective precipitation requires the degree of supersaturation in the crystallizer to be high enough, i.e. the residence time of the liquid to be short enough, for sufficiently fast nucleation and growth rates. Nucleation should produce the right amount of new crystals making up for those removed in the product stream S4. This trade-off could be addressed by crushing a small part of the solid product and feed it back into R3 as seeds, so as crystal growth could take place at a Mg-concentration level close to solubility and the basic-hydrated Mg-carbonate. In the example of Fig. 9b, the latter solubility is 90 times lower than that of nesquehonite in the dissolution reactor, which yields a large Mg-concentration difference between the liquid streams L1 and L2 that can be exploited to fix CO<sub>2</sub> in such a combined  $T$ -swing and  $p$ CO<sub>2</sub>-swing process scheme.

## 5 Double-step carbonation

The feasibility of the proposed double-step mineralization process was investigated by running simulations and by performing proof-of-principle experiments that were dedicated to the different steps of the overall process. Hereafter, we first report the outcome from a sensitivity analysis of the process and illustrative simulations for different operating modes of the dissolution reactor, before showing and analyzing the results of the corresponding experimental campaign.

### 5.1 Assessment of the process feasibility by simulations

To assess the feasibility of the double-step process by simulations, the material balance equations for the process at steady state were written and solved. To this end, the following assumptions were made for the sake of simplicity: 1) the dissolution of serpentine takes place in a single reactor R1, operated at a temperature  $T_{R1}$  of 30 °C and total pressure  $P_{R1}$  of 5 bar (the reactor R2 is not considered in these simplified calculations); the precipitator is operated at a temperature  $T_{R3}$  of 90 °C and total pressure  $P_{R3}$  of 1 bar; 2) the flue gas stream G1 has a composition of 10 % CO<sub>2</sub> and 90 % N<sub>2</sub>; 3) the mass flow rate of water in stream L1 is twenty times the gas flow rate in G1; 4) the solid phases formed in the reactor R3 are hydromagnesite and quartz; 5) the solutes in liquid stream L2 leaving the reactor R3 are at equilibrium with the solid phases therein; 6) vapor-liquid equilibrium (VLE) prevails in both reactors, R1 and R3.

A sensitivity analysis was performed to understand the effect of the steady state Mg-concentration leaving the reactor R1,  $c_{Mg}^{L1}$ , on the process performance parameters, namely the compositions of the various gas streams and the CO<sub>2</sub> captured from the flue gas. These results are shown in Fig 10a and Fig 10b, respectively. For a 10 % CO<sub>2</sub> flue gas stream G1 that

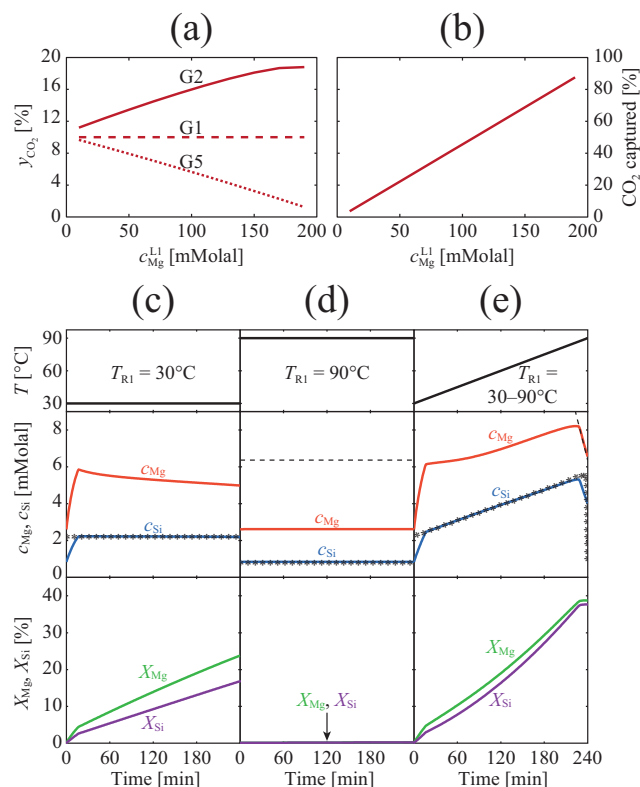


**Fig. 10** Sensitivity analysis and illustrative simulations for a combined  $T$ - $p$ CO<sub>2</sub>-swing process: Effect of the Mg-concentration attained in the dissolution reactor R1 on the (a) CO<sub>2</sub> fraction,  $y_{CO_2}$ , in the gas streams G2 (solid line), G1 (dashed line), and G5 (dotted line), as well as on the (b) CO<sub>2</sub> capture rate. Effect of different operating modes in reactor R1 of (c)  $T_{R1} = 30^\circ\text{C}$ , (d)  $T_{R1} = 90^\circ\text{C}$ , and (e) a linear temperature ramp with  $T_{R1} = 30\text{--}90^\circ\text{C}$  on the Mg-concentration (orange lines) and Si-concentration (blue lines), as well as on the Mg and Si extraction efficiency,  $X_{Mg}$  (green lines) and Si,  $X_{Si}$  (purple lines), respectively. The dashed black lines in (d,e) correspond to the Mg solubility concentration of hydromagnesite (the solubility of nesquehonite in (a) is out of scale). The line of black stars in (c-e) correspond to the Si solubility concentration of amorphous silica or quartz, depending on  $T$ .

enters the precipitator, with increasing  $c_{Mg}^{L1}$  we observe a depletion of CO<sub>2</sub> from the gas stream G5 that exits the reactor R1 and a CO<sub>2</sub> enrichment of the gas stream G2. This is favorable as it then requires less compression work to achieve an elevated  $p$ CO<sub>2</sub> for dissolution. The CO<sub>2</sub> reduction in G5 results in an increasing amount of CO<sub>2</sub> captured. It is important to realize that the percentage of CO<sub>2</sub> captured at steady state is directly related to the rate of production of hydromagnesite in the precipitator. By assuming VLE condition in the two reactors and complete precipitation of hydromagnesite and quartz in precipitator R3, the CO<sub>2</sub> captured in Fig 10b represents the

ideal (maximum) capture efficiency of this process.

In order to highlight the effect of different operating modes on the dissolution efficiency — in particular to challenge the conjectured benefit of having multiple dissolution steps at increasing  $T$  — illustrative simulations were performed for the dissolution of the PDL material in a flow-through reactor. Although the concentrations of solutes that needed to be achieved were high, the far-from-equilibrium dissolution kinetics that we had developed earlier<sup>27</sup> were nevertheless used for the sake of illustration. The dissolution of a 1 % slurry solution of PDL under a  $p\text{CO}_2$  of 1 bar was simulated. The simulations were performed based on the following assumptions: 1) VLE is assumed and computed using the same techniques described elsewhere,<sup>26</sup> while the dynamic evolution of the pH of the solution is calculated using EQ3/6<sup>39</sup>; 2) the liquid-flow through reactor is considered to have a liquid residence time of 30 min; 3) the liquid entering the dissolution reactor (L2) is assumed to have compositions that are at equilibrium with hydromagnesite and quartz at 90 °C and a mildly enriched gas stream G2 having  $p\text{CO}_2 = 0.14\text{ bar}$  ( $c_{\text{Mg}}^{\text{L2}} = 2.59\text{ mMolal}$  and  $c_{\text{Si}}^{\text{L2}} = 0.82\text{ mMolal}$ ); 4) In order to account for the passivation of the dissolving particles due to silica or carbonate precipitation, the dissolution of the particles was made possible only when the liquid composition of the solutes in the reactor is below the solubility values of the relevant silica or carbonate species; 5) nesquehonite and hydromagnesite were considered the kinetically relevant precipitating carbonate species at  $T < 60\text{ °C}$  and at  $T \geq 60\text{ °C}$ , respectively; 6) amorphous silica and quartz were considered the kinetically relevant precipitating Si species at  $T < 90\text{ °C}$  and at  $T \geq 90\text{ °C}$ , respectively. Simulations were performed for dissolution at 30 °C, at 90 °C, and for a linear temperature ramp between 30 °C and 90 °C. The simulation time was limited to 240 min. Fig 10c–e show the results of these simulations, namely the concentrations and extents of dissolution profiles for Mg and Si over time. At 30 °C, the liquid stream entering the dissolution reactor (L2) is undersaturated with respect to amorphous silica and nesquehonite at the operating conditions of the dissolution reactor. Hence the dissolution of the PDL initially starts unhindered by passivation effects. After 18 min, the Si concentration in the reactor attains the solubility limit for amorphous silica, which results in an inhibition of dissolution. Further dissolution of the serpentine particle occurs at a rate, whose maximum value is governed by the rate of Si removal through the liquid stream L1. This inhibitory effect is seen as the discontinuity in the concentration and conversion profiles of Mg and Si at 18 min in Fig. 10c. In the case of dissolution at 90 °C, the process is based only on a  $p\text{CO}_2$ -swing operation. The solution entering the reactor is mildly supersaturated with respect to quartz at the operating conditions (silica solubility decreases with  $p\text{CO}_2$  by a small extent). This results in complete inhibition of dissolution over the entire duration of the simu-

lations. As a result, the simulations yield no dissolution of the particles at this temperature.

In the case of a temperature ramp from 30 °C to 90 °C, increasing temperature results in increasing solubility values of amorphous silica and higher dissolution rates for PDL. The system reaches amorphous silica solubility in 17 min, and further dissolution of the particles is a result of the combined effects of increasing solubilities of amorphous silica and higher dissolution extents with temperature, and continuous silica removal through the liquid stream L1. This results in an overall higher extent of dissolution of the PDL particles. In Fig. 10e we also observe that at about 230 min into dissolution, the solubility of hydromagnesite inhibits the dissolution of the serpentine particles. While the actual temperature profile for the particles needs to be optimized for the system after a thorough understanding of the reaction kinetics, we are able to show that a simple linear temperature ramp by itself can result in enhanced dissolution efficiency.

## 5.2 Double-step carbonation experiments

A total of seven proof-of-principle experiments were performed using the two interconnected Teflon reactors (*cf.* Fig. 1). Note that this experimental campaign does not yet represent a complete parametric study, but rather a first insight into the performance of the proposed double-step process. The experimental conditions are reported in Table 1, together with the key data collected from these experiments.

Starting from experiment DS2, the particle size of the PDL and then the  $\text{CO}_2$  content of the feed gas in the precipitator were reduced, which, together with the use of carbonate seeds, was aimed at successively tuning these parameters towards higher efficiencies. Up to experiment DS4 the temperature in the dissolution reactor was kept constant at 30 °C to demonstrate a  $T$ -swing and  $p\text{CO}_2$ -swing with only one dissolution step. Then, temperature ramps from 30 °C to 90 °C were applied in the dissolution reactor, namely a linear ramp in DS5 and a stepwise ramp in DS6. The last two experiments DS7 and DS8 were run at 90 °C dissolution temperature, to carry out an operation driven only by  $p\text{CO}_2$ -swing.

As follows from Table 1, a lower amount of PDL ( $S/L = 1\text{ % wt.}$ ), together with the continuous withdrawal of Mg, was indeed effective in controlling the pH in the dissolution reactor. In particular, these measures helped in preventing the peaking of the pH typically observed after the start of a single-step experiments (see for instance Fig.4a). This was true for all experiments, with the exception of the two at 90 °C dissolution temperature, at which the dissolution kinetics are faster and the  $\text{CO}_2$  solubility is lower compared to the others (see also the complete pH profiles in Fig. S2<sup>†</sup>). None of the experiments showed signs of carbonation of the PDL already inside the dissolution reactor, while the product col-

lected in the precipitator consisted of pure basic-hydrated Mg-carbonate showing rosettes with a honeycomb texture of platy crystals that are characteristic for this type of carbonates.<sup>33,34,40</sup> The results from the characterization analyses performed on these solids is provided in Appendix C<sup>†</sup>.

**Table 1** Experimental conditions of the double-step carbonation experiments together with key data collected from these experiments

Exp. Nr.	Dissolution reactor at 100 % CO <sub>2</sub> , S/L = 1 % wt.						Precipitator at T = 90 °C						Process	
	T [°C]	Par. size [μm]	pH <sub>max</sub> @ t <sub>reached</sub> [-]	pH final [-]	c <sub>Mg</sub> [mm]	c <sub>Si</sub> [mm]	CO <sub>2</sub> feed [%]	Seed mass [mg]	pH <sub>max</sub> @ t <sub>reached</sub> [-]	pH final [-]	c <sub>Mg</sub> [mm]	c <sub>Si</sub> [mm]	X <sub>Mg</sub> [%]	R <sub>x</sub> [%]
DS2	30	-125	6.34 @ 73'	6.15	15.0	3.0	10	0	7.86 @ 85'	7.69	14.3	2.9	40.1	12.6
DS3	30	-125	6.46 @ 42'	6.13	11.9	2.2	0	200	7.92 @ 10'	7.74	11.1	1.8	44.1	22.4
DS4	30	-20	6.63 @ 6'	6.07	11.0	2.1	0	200	7.88 @ 10'	7.72	10.6	1.7	45.7	25.3
DS5	30-90	-20	6.89 @ 234'	6.87	8.6	3.8	0	200	7.90 @ 240'	7.90	7.1	1.7	50.2	35.6
DS6	30/50/60/90	-20	7.14 @ 197'	6.85	8.2	3.6	0	200	7.97 @ 212'	7.94	6.5	1.6	48.5	34.9
DS7	90	-20	8.21 @ 1'	6.79	7.9	1.5	0	200	8.23 @ 10'	8.02	7.0	0.7	38.9	25.2
DS8	90	-20	8.20 @ 1'	6.85	9.0	1.8	0	100	8.32 @ 9'	8.02	7.9	1.0	35.5	20.0

The efficiency achieved in experiment DS2 can be compared to that in the 30 °C single-step experiment with S/L = 5 % wt., since both experiments used the PDL particle size fraction of under 125 μm. Despite its five times lower S/L ratio, experiment DS2 reached a level of R<sub>x</sub> of 12.6 %, while virtually no carbonation took place in the single-step case (*cf.* Fig. 6c).

If seeds were used in the precipitator of the real process, their rate of supply would have to be chosen carefully. This can be appreciated by comparing the carbonation efficiency between experiments DS2 and DS3, as well as between DS7 and DS8, where the amount of seeds was changed from zero to 200 mg and from 200 mg to 100 mg, respectively. In fact, R<sub>x</sub> almost doubled between the unseeded and seeded experiment under otherwise equal conditions.

**5.2.1 Effect of dissolution temperature.** For the sake of clarity, the solute concentration data along with the process efficiency of experiments DS4-7 is plotted in Fig. 11, to make a detailed analysis of the effect of the dissolution temperature possible. The calculated solubility levels provided in Fig. 11a,b span a range that goes from the two extreme cases of assuming the reactor solution to be at equilibrium with pure CO<sub>2</sub> or with a gas containing only 1 % CO<sub>2</sub>. This is because the incoming liquid was either leaner or richer in dissolved CO<sub>2</sub> than the reactor solution at equilibrium with the two different feed gases used in these experiments (100 % CO<sub>2</sub> in the dissolution reactor, 0 % CO<sub>2</sub> in the precipitator). The given range could only be narrowed down if the prevailing gas-liquid and liquid-gas transfer kinetics were known.

The final Mg-concentration in the precipitator (Fig. 11a) was almost four times lower than the level measured in the 90 °C single-step experiments (*cf.* Fig. 7d). This indicates that, as desired, the stripping of the incoming dissolved CO<sub>2</sub> from the solution was at least partly effective, thus lowering the apparent solubility of the basic-hydrate Mg-carbonate observed in our experiments. The difference in the Mg-concentration between the precipitator and the dissolution reactor is only marginal. Apparently, while precipitation was fast enough to consume the incoming Mg, the extraction of make-up Mg in the dissolution reactor must have been indeed slow, at least towards the end of the experiments.

Somewhat more pronounced is the difference in the Si-concentration between the two reactors, especially for the two T-ramp experiments (Fig. 11b). Despite the final temperature in the dissolution reactor of 90 °C, the Si-concentration therein was higher than the calculated solubility range of quartz and only a little below that of amorphous silica. During these runs, silica re-precipitated at lower temperatures, *i.e.* in the form of amorphous silica. Apparently the full transformation of the latter into quartz and the corresponding reduction of the Si-concentration level could not take place yet, due to kinetic limitations.

The Si-concentration at the end of experiment DS4 ( $T$ -swing) was close to the calculated amorphous silica solubility range. This is in contrast to the low-S/L single-step experiment at 30 °C, where the Si-concentration after 240 min was three times higher than the amorphous silica solubility (cf. Fig. 6a), but again fits into the picture gained from the illustrative simulations (cf. Fig. 10c).

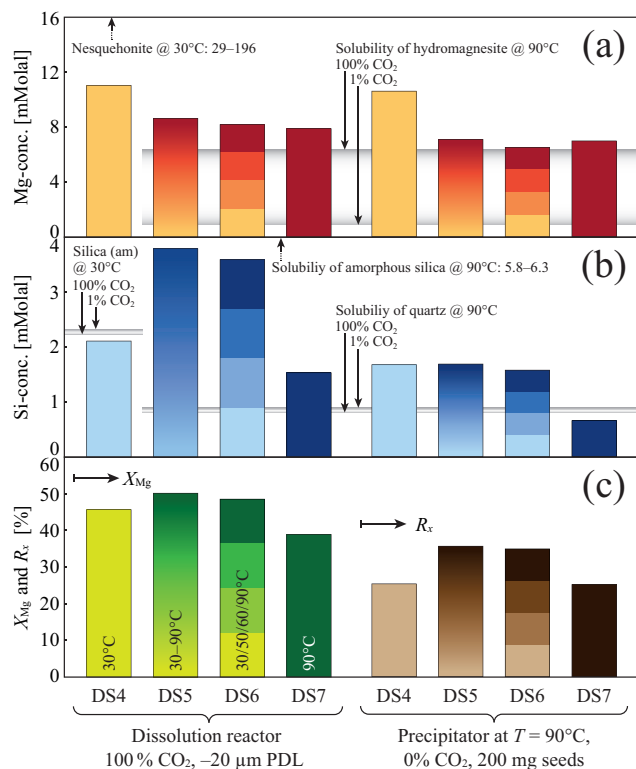


**Fig. 11** Double-step carbonation experiments DS4-7: (a) Final Mg-concentration (orange) and (b) Si-concentration (blue) in the dissolution reactor (left) and in the precipitator (right), together with the (c) overall process efficiency in terms of the extent of dissolution (green) and carbonation (brown),  $X_{Mg}$  and  $R_c$ , respectively. The color intensity of the bars reflect the operating mode with respect to the temperature in the dissolution reactor from 30 °C (faint) to 90 °C (intense). The horizontal gray bars indicate the calculated solubility level for the relevant precipitates over a large range of  $pCO_2$  (see text).

Among the four experiments, the final Si-concentration of DS7 ( $pCO_2$ -swing only) was closest to the calculated solubility of quartz in both reactors. This gives reason to assume that during this experiment, the re-precipitated Si-layer was furthest developed. Indeed, this experiment was least efficient with regard to the measured Mg-extraction (Fig. 11c). Moreover, throughout this experiment, the pH in the dissolution reactor was between 0.7 and 1.6 pH units higher than the pH measured for the  $T$ -swing experiment (see also Fig. S2<sup>†</sup>). As

in the case of the single-step experiments, this may have been an additional handicap for efficient Mg-extraction, especially at the beginning when dissolution was likely to be not yet hindered by a passivating Si-rich layer.

In general, as follows from Table 1 and Fig. 11c, the highest values of  $X_{Mg} = 50.2\%$  and of  $R_c = 35.6\%$  that were attained in this campaign occurred during one of the experiments with a  $T$ -ramp in the dissolution reactor, followed by the  $T$ -swing experiments and those driven only by  $pCO_2$ -swing. The same ranking was found from the illustrative simulations reported in Subsection 5.1. Thus, the underlying assumptions for these simulations appear reasonable. Although, the generally higher dissolution efficiencies observed in the experiments indicate that the assumption of a complete inhibition of dissolution once the dissolution reactor reaches the quartz, amorphous silica, or carbonate solubility was over-pessimistic.

## 6 Conclusions and implications

In this study, we could demonstrate for the first time that a natural silicate mineral can be carbonated under lean operating conditions, without the use of pH-tuning agents, and at time scales that are relevant for an industrial application. Generally low process efficiencies were observed for single-step batch experiments with partially dehydroxylated lizardite reacting in an aqueous medium under a gas flow of pure CO<sub>2</sub> and up to temperatures of 90 °C. These were addressed by concurrent grinding to create fresh reactive surface, and by separating the dissolution step from the precipitation step in a double-step scheme. The decreasing solubility of carbonates with temperature — together with the peculiar precipitation kinetics in the Mg-carbonate system that lead to different forms of differently soluble metastable compounds within a small range of temperatures — makes it possible to exploit a temperature swing to achieve the goal of selective precipitation. In combination with a  $pCO_2$ -swing, the formation of Mg-carbonates is promoted at low  $pCO_2$  and correspondingly higher pH in the precipitator, whereas Mg-extraction in the dissolution reactor can benefit from the acidity provided by a slightly elevated  $pCO_2$ .

The feasibility of this concept was assessed by simulations and through experiments, yielding a pure basic-hydrated Mg-carbonate as the product. Both assessment approaches confirmed the presumed benefit of multiple dissolution steps at increasing temperature. Up to 50% Mg-extraction efficiency was achieved in the dissolution reactor using a feed gas of pure CO<sub>2</sub> at atmospheric pressure to simulate a moderately pressurized flue gas. The Mg-extraction efficiency determines the overall process efficiency with respect to the solid feed, since in a continuous process, all Mg that enters the solution will eventually be converted into a carbonate. In conclusion, the assessment showed that the process concept of a combined

$T$ - $p\text{CO}_2$ -swing can be considered robust.

To further maximize the process efficiency, future work needs to find ways to circumvent the passivation of the reactive surface by Si re-precipitation. Under the constraint of avoiding the use of chemical additives, two options bear potential. First, following from the observed positive effect of concurrent grinding on the onset of precipitation and the process efficiency during the single-step experiments, the slurry in the dissolution reactor could be fluidized together with an internal grinding medium by introducing and partly recirculating the flue gas stream from the bottom — similar to the method described in Park *et al.*<sup>41</sup>. Secondly, the Si-rich effluent from each dissolution reactor, after exchanging heat, could be passed through a packed bed of amorphous silica, or into separate tanks containing these materials as seeds, to achieve suitably long residence times. Alternatively, silica with a high specific surface area could be mounted on static elements such as rods or sheets, which are plunged into the dissolution reactors and can be frequently replaced. A cooling fluid could be passed through the interior of these elements to increase the driving force of Si re-precipitation onto their surface instead of onto that of the dissolving feed. Either alternative could allow to spatially separate the Si-precipitation from the activated serpentine slurry, thereby also increasing the purity of the Mg-carbonate in the precipitator and offering the possibility of harvesting silica as a side-product.

This study shows that there is a route to flue gas mineralization using activated serpentine. The proposed process has an energy penalty and heat integration profile that is completely different from that of post-combustion capture, transport, and geological storage, *i.e.* the value chain links of conventional CCS. Amine capture requires high-grade heat for solvent regeneration and electrical power for the compression of a small amount of gas ( $\text{CO}_2$  only) up to a high pressure level, the latter being the enabling element for subsequent storage. Our flue gas mineralization route requires low-grade heat to warm up the liquid and electric power to compress a big amount of gas (all flue gases) up to a low pressure level. Here, the enabling element is the thermal pretreatment of the serpentine. The quantitative contributions to the overall energy penalty will depend on the operating conditions and the residence times of the various streams. Hence, the ultimate performance will be the outcome of a complex optimization process, which is subject of ongoing work.

## Acknowledgments

Financial support from the Foundation Claude & Giuliana (Basel, CH), from the Swiss National Science Foundation, and from the competence centers CCEM - Energy & Mobility and CCES - Environment & Sustainability (both of the ETH domain, CH) is gratefully acknowledged. We thank Daniela Zin-

garetti and Renato Baciocchi from the University of Rome Tor Vergata for providing TIC service and for supporting us during the experimental test phase antecedent to this study, as well as Markus Hänchen from ETH Zurich for his valuable input during discussions.

## Notation

$c$	aqueous concentration of solute [ $\text{mol kg}^{-1}$ ]
$C$	mass correction parameter for $x_{\text{CO}_2}$ in Eq. 1 [-]
$i$	sample index ( $i = 1, \dots, 8$ )
$m_l$	mass of liquid phase [g]
$m_s$	mass of solid phase [g]
$m_{\text{seed}}$	mass of seeds [g]
$M$	molar mass [ $\text{g mol}^{-1}$ ]
$n_{\text{Mg},0}$	moles of Mg in PDL feed added at $t = 0$ [mol]
$n_{\text{Mg},l}$	moles of Mg in liquid phase [mol]
$p\text{CO}_2$	partial pressure of $\text{CO}_2$ [bar]
$P$	total pressure [bar]
$r$	ratio between Mg and $\text{CO}_2$ of a Mg-carbonate [-]
$R_x$	extent of carbonation (carbonation efficiency) [%]
$S/L$	Solid to liquid ratio (slurry density) [% wt.]
$t$	time [min]
$t_{\text{onset}}$	time corresponding to onset of precipitation [min]
$T$	temperature [ $^{\circ}\text{C}$ ]
$x_{\text{CO}_2}$	mass fraction of $\text{CO}_2$ in a TGA sample [%]
$x_{\text{Mg},0}$	mass fraction of Mg in the PDL [%]
$X$	extent of dissolution (extraction efficiency) [%]
$y_{\text{CO}_2}$	mole fraction of $\text{CO}_2$ [%]
$z$	degree of hydration of a basic-hydrated Mg-carbonate ( $4 \leq z \leq 11$ ) [-]

## Acronyms

CCS	Carbon dioxide capture and storage
CCU	Carbon dioxide capture and utilization
EDX	Energy-dispersive X-ray spectroscopy
PDL	Partially dehydroxylated lizardite
SEM	Scanning electron microscope
SGSI	Shell Global Solutions International
TGA	Thermogravimetric analysis
VLE	Vapor-liquid equilibrium
XRD	X-ray diffraction

## References

- M. Mikkelsen, M. Jørgensen and F. C. Krebs, *Energ. Environ. Sci.*, 2010, **3**, 43–81.
- B. M. Bhanage and M. Arai, *Transformation and Utilization of Carbon Dioxide*, Springer Berlin, 2014.
- IPCC, *IPCC special report on carbon dioxide capture and storage. Prepared by Working Group III of the Intergovernmental Panel on Climate Change*, Cambridge University Press, United Kingdom and New York, NY, USA, 2005, p. 442.

- 4 L. Hollingbery and T. Hull, *Thermochimi. Ac.*, 2010, **509**, 1–11.
- 5 L. Haurie, A. I. Fernández, J. I. Velasco, J. M. Chimenos, J.-M. Lopez Cuesta and F. Espiell, *Polym. Degrad. Stabil.*, 2006, **91**, 989–994.
- 6 W. K. O'Connor, D. C. Dahlin, G. E. Rush, S. J. Gerdemann, L. R. Penner and D. N. Nilsen, *Aqueous mineral carbonation: Mineral availability, pre-treatment, reaction parametrics, and process studies*, Albany Research Center Technical Report DOE/ARC-TR-04-002, Final Project Report, 2005.
- 7 W. J. J. Huijgen, G.-J. Witkamp and R. N. J. Comans, *Chem. Eng. Sci.*, 2006, **61**, 4242–4251.
- 8 A. V. Chizmeshya, M. J. McKelvy, K. Squires, R. W. Carpenter and H. Bearat, *A novel approach to mineral carbonation: Enhancing carbonation while avoiding mineral pretreatment process cost*, Arizona State University Technical Report DE-FG26-04NT42124, 2007.
- 9 H. Geerlings and R. Zevenhoven, *Annu. Rev. Chem. Biomolec. Eng.*, 2013, **4**, 103–117.
- 10 X. Wang and M. M. Maroto-Valer, *ChemSusChem*, 2011, **4**, 1291–1300.
- 11 R. Zevenhoven, J. Fagerlund and J. K. Songok, *Greenh. Gas. Sci. Technol.*, 2011, **1**, 48–57.
- 12 W. K. O'Connor, D. C. Dahlin, G. E. Rush, S. J. Gerdemann and L. R. Penner, 7th International Conference on Greenhouse Gas Control Technologies, 2004.
- 13 S. J. Gerdemann, W. K. O'Connor, D. C. Dahlin, L. R. Penner and H. Rush, *Environ. Sci. Technol.*, 2007, **41**, 2587–2593.
- 14 J. J. C. Geerlings, G. A. F. van Mossel and B. C. M. in't Veen, *Process for producing CaCO<sub>3</sub> or MgCO<sub>3</sub>*, 2006, WO2006008242(A1).
- 15 J. J. C. Geerlings and E. Wesker, *A process for sequestration of carbon dioxide by mineral carbonation*, 2008, WO2008142017(A2)(A3).
- 16 M. A. Verduyn, H. Boerrigter, R. Oudwater and G. A. F. van Mossel, 5th Trondheim Conference on CO<sub>2</sub> Capture, Transport, and Storage, 2009.
- 17 R. D. Balucan, B. Z. Dlugogorski, E. M. Kennedy, I. V. Belova and G. E. Murch, *Int. J. Greenh. Gas Con.*, 2013, **17**, 225–239.
- 18 R. D. Balucan, E. M. Kennedy, J. F. Mackie and B. Z. Dlugogorski, *Greenh. Gas. Sci. Technol.*, 2011, **1**, 294–304.
- 19 R. D. Balucan and B. Z. Dlugogorski, *Environ. Sci. Technol.*, 2012, **47**, 182–190.
- 20 M. Ghoorah, B. Z. Dlugogorski, H. C. Oskierski and E. M. Kennedy, *Miner. Eng.*, 2014, **59**, 17–30.
- 21 K. Alizadehhesari, S. D. Golding and S. K. Bhatia, *Energ. Fuel.*, 2012, **26**, 783–790.
- 22 K. M. Steel, K. Alizadehhesari, R. D. Balucan and B. Bašić, *Fuel*, 2013, **111**, 40–47.
- 23 W. Li, W. Li, B. Li and Z. Bai, *Chem. Eng. Res. Des.*, 2009, **87**, 210–215.
- 24 T. Björklöf and R. Zevenhoven, *Chem. Eng. Res. Des.*, 2012, **90**, 1467–1472.
- 25 L.-C. Pasquier, G. Mercier, J.-F. Blais, E. Cecchi and S. Kentish, *Environ. Sci. Technol.*, 2014, **48**, 5163–5170.
- 26 M. Werner, S. Hariharan, D. Zingaretti, R. Baciocchi and M. Mazzotti, *Chem. Eng. J.*, 2014, **241**, 301–313.
- 27 S. Hariharan, M. Werner, M. Hänchen and M. Mazzotti, *Chem. Eng. J.*, 2014, **241**, 314–326.
- 28 M. Werner, S. B. Hariharan, A. V. Bortolan, D. Zingaretti, R. Baciocchi and M. Mazzotti, *Energy Procedia*, 2013, **37**, 5929–5937.
- 29 M. Hänchen, V. Prigiobbe, R. Baciocchi and M. Mazzotti, *Chem. Eng. Sci.*, 2008, **63**, 1012–1028.
- 30 Z. Zhang, Y. Zheng, Y. Ni, Z. Liu, J. Chen and X. Liang, *J. Phys. Chem. B*, 2006, **110**, 12969–12973.
- 31 P. J. Davies and B. Bubela, *Chem. Geol.*, 1973, **12**, 289–300.
- 32 J. H. Canterford, G. Tsambourakis and B. Lambert, *Mineral. Mag.*, 1984, **48**, 437–42.
- 33 L. Hopkinson, P. Kristova, K. Rutt and G. Cressey, *Geochim. Cosmochim. Ac.*, 2012, **76**, 1–13.
- 34 P. Ballirano, C. De Vito, S. Mignardi and V. Ferrini, *Chem. Geol.*, 2013, **340**, 59–67.
- 35 V. Vágvölgyi, M. Hales, R. L. Frost, A. Locke, J. Kristóf and E. Horváth, *J. Therm. Anal. Calorim.*, 2008, **94**, 523–528.
- 36 V. Vágvölgyi, R. L. Frost, M. Hales, A. Locke, J. Kristóf and E. Horváth, *J. Therm. Anal. Calorim.*, 2008, **92**, 893–897.
- 37 S. Teir, S. Eloneva, C.-J. Fogelholm and R. Zevenhoven, *Appl. Energ.*, 2009, **86**, 214–218.
- 38 V. Ferrini, C. De Vito and S. Mignardi, *J. Hazard. Mater.*, 2009, **168**, 832–837.
- 39 T. J. Wolery and R. L. Jarek, *Software user's manual, EQ3/6, Version 8.0*, Sandia national laboratories technical report, 2003.
- 40 L. Hopkinson, K. Rutt and G. Cressey, *J. Geol.*, 2008, **116**, 387–400.
- 41 A.-H. A. Park and L.-S. Fan, *Chem. Eng. Sci.*, 2004, **59**, 5241–5247.